Low-Temperature Plasma-Assisted Atomic-Layer-Deposited SnO₂ as an Electron Transport Layer in Planar Perovskite Solar Cells

Yinghuan Kuang,[†,⊥] Valerio Zardetto,[‡,§] Roderick van Gils,[†] Saurabh Karwal,[†] Dibyashree Koushik,[†] Marcel A. Verheijen,[†,∥] Lachlan E. Black,[†] Christ Weijtens,[†] Sjoerd Veenstra,[§] Ronn Andriessen,[‡,§] Wilhelmus M.M. Kessels,[†,§] and Mariadriana Creatore*[,†,§]

[†]Department of Applied Physics, Eindhoven University of Technology (TU/e), 5600 MB Eindhoven, The Netherlands
[‡]TNO, High Tech Campus 21, 5656 AE Eindhoven, The Netherlands
[§]Solliance, High Tech Campus 21, 5656 AE Eindhoven, The Netherlands
[∥]Philips Innovation Labs, High Tech Campus 11, 5656 AE Eindhoven, The Netherlands

Ⓢ *Supporting Information*

ABSTRACT: In this work, we present an extensive characterization of plasma-assisted atomic-layer-deposited SnO₂ layers, with the aim of identifying key material properties of SnO₂ to serve as an efficient electron transport layer in perovskite solar cells (PSCs). Electrically resistive SnO₂ films are fabricated at 50 °C, while a SnO₂ film with a low electrical resistivity of 1.8×10^{-3} Ω cm, a carrier density of 9.6×10^{19} cm⁻³, and a high mobility of 36.0 cm²/V s is deposited at 200 °C. Ultraviolet photoelectron spectroscopy indicates a conduction band offset of ∼0.69 eV at the 50 °C SnO₂/Cs₀.₀₅(MA₀.₁₇FA₀.₈₃)₀.₉₅Pb-(I₂.₇Br₀.₃) interface. In contrast, a negligible conduction band offset is found between the 200 °C SnO₂ and the perovskite. Surprisingly, comparable initial power conversion efficiencies (PCEs) of 17.5 and 17.8% are demonstrated for the champion cells using 15 nm thick SnO₂ deposited at 50 and 200 °C, respectively. The latter gains in fill factor but loses in open-circuit voltage. Markedly, PSCs using the 200 °C compact SnO₂ retain their initial performance at the maximum power point over 16 h under continuous one-sun illumination in inert atmosphere. Instead, the cell with the 50 °C SnO₂ shows a decrease in PCE of approximately 50%.

KEYWORDS: *tin oxide, atomic layer deposition, perovskite solar cells, stability, interface, inorganic electron transport layer*
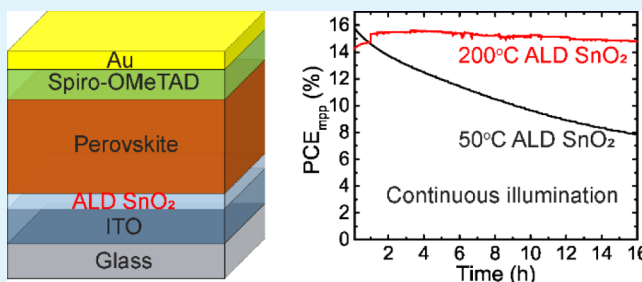
1. INTRODUCTION

Over a relatively short development period of about eight years, the initial efficiency of perovskite solar cells (PSCs) has rocketed from 3.8% in 2009 up to a record efficiency of 23.3% at a laboratory scale in 2018.[1,2] This high energy conversion efficiency combined with a potentially low fabrication cost makes this technology highly promising for future photovoltaic (PV) electricity generation applications.[3] Methylammonium (CH₃NH₃⁺, MA) lead tri-iodide (MAPbI₃) is extensively adopted as photo-absorber in PSCs. Despite the impressive initial performance, critical issues remain which hamper the industrial application of this material. Among these, environmental instability due to decomposition in contact with moisture,[4−8] thermal instability due to the structural transition and volatile nature of the decomposed components at elevated temperatures,[9−15] and light instability due to ion migration upon illumination[16−18] are the main concerns. Enormous efforts are presently being made to overcome these intrinsic challenges. One of the most successful strategies so far is the change of the perovskite chemical composition to a mixed-cation lead mixed-halide formula. For instance, the MA cation can be partially substituted by formamidinium (FA,

CH₃(NH₂)₂⁺) to form a MA/FA dual cation perovskite. Furthermore, cesium (Cs⁺)[19] and rubidium ions (Rb⁺)[20] can contribute to the synthesis of Cs/MA/FA triple and Rb/Cs/MA/FA quadruple cation perovskites. As for the mixed halide anions, bromide is typically introduced to form mixed anions I⁻/Br⁻. In this way, stability has been enhanced. Furthermore, the increased optical band gap makes it a promising top cell candidate in a tandem device for better exploitation of the solar spectrum.

To achieve an efficient electron collection in PSCs, the electron transport layer (ETL) is of crucial importance. General requirements for ETLs are considered to include the following: (1) a negligible conduction band offset with perovskites for fast electron extraction and, simultaneously, a sufficiently large valence band (VB) offset for hole blocking at the ETL/perovskite interface; (2) a pin-hole-free structure to avoid shunts due to direct contact between perovskites and electrodes; (3) a high electron mobility for fast charge

transport and a good electrical conductivity for minimal series resistance; and (4) excellent optical transparency. Titanium dioxide (TiO$_2$) has traditionally been employed as the ETL for MAPbI$_3$ PSCs,[1] as PSCs historically evolved from dye-sensitized solar cells.[21,22] However, TiO$_2$ suffers from UV instability upon AM1.5 illumination.[23,24] In addition, it has been reported in several works that TiO$_2$ thin films possess an unfavorable conduction band minimum (CBM) alignment with mixed cation perovskites, which consequently hinders an efficient electron extraction at the TiO$_2$/perovskite interface.[25,26] In contrast to TiO$_2$, SnO$_2$ is characterized by a deeper CBM and valence band maximum (VBM), compatible with the aim of an efficient electron extraction while blocking hole transport.[25] Besides the favorable energy levels, SnO$_2$ possesses a larger optical band gap in the range of 3.6–4.4 eV. These excellent optoelectronic properties make SnO$_2$ a promising electron transport material, particularly for mixed cation PSCs.[25]

Despite these remarkable optoelectronic advantages, SnO$_2$ has only very recently been applied as the ETL for PSCs. In these early works, solution-based processes have typically been employed to fabricate mesoporous SnO$_2$ films, followed by thermal annealing.[27−33] Atomic layer deposition (ALD), on the other hand, can deliver high-quality pin-hole-free metal oxides even at low substrate temperatures. The thickness can be accurately controlled at the ångström level because of self-limiting surface reaction mechanisms.[34−37] ALD processes for the synthesis of SnO$_2$ films have previously been reported using halogenated precursors SnCl$_4$[38−41] and SnI$_4$.[41,42] The corrosive precursors and the HCl byproduct, the relatively high deposition temperature of typically >300 °C, and the relatively low growth per cycle (GPC) are the main concerns limiting the applications of these precursors. In this regard, a halogen-free precursor, tetrakis(dimethylamino)tin (TDMASn), for atomic-layer-deposited SnO$_2$ was first investigated by Elam et al.[43] H$_2$O$_2$, H$_2$O, and O$_3$ were tested as the oxidation sources. Following that work, H$_2$O$_2$,[44,45] H$_2$O vapor,[46] and O$_3$[47,48] have been used as co-reactants. More recently, O$_2$ plasma-assisted ALD of SnO$_2$ has also been reported.[49,50] The use of O$_2$ plasma reactant allows for low temperatures for SnO$_2$ thin-film deposition.

Atomic-layer-deposited SnO$_2$ layers have recently been implemented as ETLs in PSCs, contributing to notably high solar cell performance.[24,25,49−55] So far, most of these pioneering works on atomic-layer-deposited SnO$_2$ for PSCs have focused primarily on the implementation of SnO$_2$ in PSCs and optimization of the device structure. However, understanding which material properties control the quality of the SnO$_2$/perovskite interface not only is highly relevant for achieving high-efficiency devices but can also contribute to the development of novel ETLs. In this regard, a very recent work by Lee et al. demonstrates that surface passivation of SnO$_2$ for reduced interfacial recombination, accompanied by post-annealing to improve electrical properties and in combination with compact TiO$_2$ layer for enhanced hole blocking, is the key to achieve power conversion efficiencies (PCEs) exceeding 20% for planar n−i−p PSCs using atomic-layer-deposited SnO$_2$ as the ETL.[54] In that work, SnO$_2$ films were deposited at 100 °C using TDMASn as a tin precursor and ozone as a co-reactant. Interestingly, the SnO$_2$ film was found being self-passivated by the unreacted TDMASn in the film.[54]

In our work, instead of investigating the effect of post-annealing, we focus on the influence of deposition temperature on material properties of SnO$_2$. We report on an extensive material characterization, ranging from its chemistry to its opto-electrical and structural properties. Subsequently, we present the implementation of atomic-layer-deposited SnO$_2$ in planar n−i−p Cs$_{0.05}$(MA$_{0.17}$FA$_{0.83}$)$_{0.95}$Pb(I$_{2.7}$Br$_{0.3}$) PSCs. SnO$_2$ layers deposited at 50 and 200 °C were selected as the ETL because they exhibit very different optoelectronic properties. Surprisingly, similar initial PCEs were demonstrated for both types of SnO$_2$. Specifically, the electrically resistive SnO$_2$ deposited at 50 °C has led to higher open-circuit voltage but lower fill factor, with respect to the cells with SnO$_2$ deposited at 200 °C. The difference in cell performance is instead found when investigating the PSC stability under continuous AM1.5G illumination. The layer deposited at 200 °C enables to deliver a more stable n−i−p planar PSC because of a better charge extraction at the SnO$_2$/perovskite interface.

2. EXPERIMENTAL SECTION

2.1. Plasma-Assisted Atomic Layer Deposition of SnO$_2$. SnO$_2$ thin films were deposited at substrate temperatures of 50, 100, 150, and 200 °C on Czochralski polished c-Si (100) wafers and indium tin oxide (ITO) glass substrates in an Oxford Instruments OpAL ALD reactor using tetrakis(dimethylamino)tin (TDMASn) (99% purity, Strem Inc.) as the tin precursor and radio-frequency (RF) inductively coupled oxygen plasma as the co-reactant. The precursor bubbler was heated to 45 °C. Argon gas at a flow rate of 100 sccm was used as the carrier gas. The ALD process consists of a TDMASn dose of 2 s and subsequently a purge of 10 s, followed by an O$_2$ plasma exposure of 10 s and a purge of 5 s. Schematics for the ALD reactor and for the ALD process are shown in Figure S1. An RF power of 300 W and a pressure of 100 ± 5 mTorr (∼13 Pa) were used for the O$_2$ plasma. Prior to the SnO$_2$ depositions, the c-Si and the ITO glass substrates were cleaned by O$_2$ plasma for 3 min in the same ALD reactor using the same plasma settings used for the film deposition. GPC of 1.5, 1.2, 1.3, and 1.4 Å were determined by in situ spectroscopic ellipsometry (SE) for the films grown on c-Si at deposition temperatures of 50, 100, 150, and 200 °C, respectively (see Figure S2 in the Supporting Information).

2.2. Solar Cell Fabrication Procedure. For solar cell fabrication, soda-lime glass slides coated with ∼115 nm thick In$_2$O$_3$/Sn (ITO) layers (sheet resistance: ∼16 Ω/□, Naranjo Substrates) were used as substrates and were ultrasonically cleaned for 5 min in a sequence of detergent (Extran MA01), deionized water, and isopropanol. SnO$_2$ layers with a nominal thickness of 15 nm were deposited on the ITO substrates at a deposition temperature of either 50 or 200 °C. Shortly before perovskite deposition, the SnO$_2$ layers were pretreated with an O$_2$ plasma for 2.5 min at room temperature, using an RF power of 600 W and a pressure of ∼1 mbar.

Triple cation perovskite layers were fabricated following a recipe reported elsewhere.[19] Briefly, a precursor solution was prepared by dissolving HC(NH$_2$)$_2$I (FAI, 1 M, Greatcell Solar), PbI$_2$ (1.25 M, TCI), CH$_3$NH$_3$Br (MABr, 0.2 M, Greatcell Solar), and PbBr$_2$ (0.1 M, TCI) in anhydrous N,N-dimethylformamide (Sigma-Aldrich) and dimethyl sulfoxide (DMSO, Sigma-Aldrich) (volume ratio = 9:1). Then, 1.5 M pre-dissolved CsI (Sigma-Aldrich) solution in DMSO was added to the mixed perovskite precursor after 4 h stirring at room temperature. The perovskite solution was spin-coated onto the substrates in a two-step program at 2000 and 5000 rpm for 10 and 30 s, respectively. During the second step, 300 μL of chlorobenzene (Sigma-Aldrich) was poured on the rotating substrate 17 s prior to the end of the program. The as-deposited perovskite films were further annealed on a hotplate at 100 °C for 30 min in a nitrogen-filled glovebox.

2,2′,7,7′-Tetrakis(N,N-di-p-methoxyphenyl-amine)-9,9′-spirobi-fluorene (spiro-OMeTAD) (Lumtec Inc.) solution [80 mg/mL in chlorobenzene doped with 28.5 μL of 4-tert-butylpyridine (96%, Sigma-Aldrich) and 17.5 μL of a 520 mg/mL solution of lithium bis(trifluoromethanesulfonyl)imide (LiTFSI, 99.95%, Sigma-Aldrich)

in acetonitrile] was spin-coated onto the perovskite at 2000 rpm. The semicells were exposed to air overnight for O_2 doping of the spiro-OMeTAD. The devices were completed with a ~80 nm thick gold contact layer deposited on top of the spiro-OMeTAD via thermal evaporation at a base pressure of ~10^{-5} Torr.

2.3. Material Characterization. The composition of the SnO_2 films was examined by X-ray photoelectron spectroscopy (XPS) (K-Alpha, Thermo Fisher Scientific Inc.), and by Rutherford back-scattering spectrometry (RBS) combined with elastic recoil detection (ERD) (2 MV Tandetron, High Voltage Engineering Europe). RBS/ERD measurements were carried out by Detect99. The crystal structures of the SnO_2 and the perovskite films were analyzed using X-ray diffraction (XRD, PANalytical X'Pert PRO MRD). Optical properties, that is, refractive indices n and k, absorption coefficient α, transmission, and reflection, of SnO_2 were determined by SE (NIR Ellipsometer M2000, J.A. Woollam Co.) and UV−vis−NIR spectroscopy (Agilent Cary 5000). A Tauc−Lorentz oscillator in combination with a Drude oscillator is adopted in the modeling. The SnO_2 layers deposited on c-Si wafers coated with a ~450 nm SiO_2 layer were characterized by Hall measurements in a van der Pauw configuration (ECOPIA HMS-5300).

Ultraviolet photoelectron spectroscopy (UPS) measurements were performed in a multichamber VG EscaLab II system (Thermo Fisher Scientific Inc.) with a base pressure of ~10^{-8} Pa, using He−I radiation (21.2 eV) generated in a differentially pumped discharge lamp. A specially designed sample transport unit was used to transfer the perovskite samples from the glovebox to the UPS analysis chamber, thereby preventing possible surface modification due to air exposure. The SnO_2 samples, however, were exposed to air for ~5 min after being taken out from the ALD reactor.

Steady-state and time-resolved photoluminescence (TRPL) measurements were performed using an in-house built system. A 532 nm continuous-wave laser was used for the steady-state PL measurements, while a 635 nm pulsed laser operating at 5 MHz was used for the TRPL measurements. The laser beam entered the samples from the glass side.

Atomic force microscopy (AFM, Veeco Dimension 3100), scanning electron microscopy (SEM, FEI MK2 Helios Nanolab 600), and transmission electron microscopy (TEM) were employed to check the morphology of the layers. For TEM top-view imaging, SnO_2 films were deposited on TEM windows consisting of a SiN membrane coated with a ~5 nm thick atomic-layer-deposited SiO_2 layer. A cross-sectional lamella of the PSC was prepared using a focused ion beam (FIB) lift-out technique. To protect the top surface of the solar cell from FIB induced damage, a protective Pt layer was deposited in two steps before FIB milling. Subsequent TEM imaging was performed using a probe-corrected JEOL ARM 200, equipped with a 100 mm^2 silicon drift detector for energy-dispersive X-ray spectroscopy (EDX).

2.4. Solar Cell Characterization. $J−V$ measurements for the PSCs were measured by a Keithley 2400 source meter in a nitrogen-filled glovebox under simulated AM1.5G illumination (1000 W/m^2), using an ABET Sun 2000 Class A solar simulator. The active area was defined by a metal mask with a square opening of 0.09 cm^2. Prior to the $J−V$ measurements, the cells were illuminated for 1 min.

3. RESULTS AND DISCUSSION

3.1. Material Characterization of SnO_2. *3.1.1. Chemical Composition.* To determine the bonding states of the SnO_2 films, XPS analysis was carried out. Figure 1 shows the XPS spectra for ~30 nm thick films of 50 and 200 °C. XPS spectra for all the films deposited at 50, 100, 150, and 200 °C are shown in Figure S3. The surface of the films was sputtered by Ar ions to remove adventitious carbon. The Sn $3d_{3/2}$ peak at 495.6 eV and the Sn $3d_{5/2}$ peak at 487.0 eV, as well as the O 1s peak at 530.8 eV are assigned to SnO_2.[56,57] Because the binding energies of the Sn 3d peaks for Sn^{2+} (SnO) are only ~0.7 eV lower with respect to those for Sn^{4+} (SnO_2), the VB
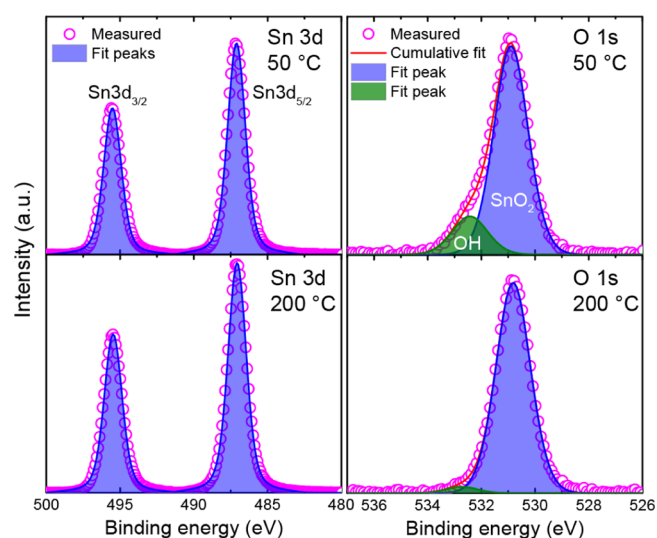
Figure 1. XPS spectra of atomic-layer-deposited SnO_2 films deposited at substrate temperatures of 50 and 200 °C.

spectra are recorded to check the presence of SnO in the film (see Figure S4a).[56,57] The Sn 5s peak located at 2.5−3 eV, which is the characteristic peak for SnO,[56] is not observed in the VB spectra for the films deposited at all temperatures. The deconvoluted O 1s peak at 532.5 eV is associated with hydroxyl oxygen (OH) species.[57] C and N contamination is also present in the film deposited at these temperatures, which can be attributed to an incomplete removal of ligands. The concentration of OH groups and of C and N contamination decreases with the increase in deposition temperature (Table 1 and Figure S3). No contamination is detected for the 200 °C film (see Figure S4b,c for the XPS survey scans).

RBS and ERD were carried out to determine the chemical composition of the films. The results are summarized in Table 1. They reveal that the film deposited at 50 °C contains a remarkably high H fraction of 20 at. %. As previously concluded from the XPS results (Figure 1), hydrogen probably mainly stems from the OH groups bonded to Sn and C. The H concentration decreases upon increasing the deposition temperature. Neither C nor N is detected by RBS. The O/Sn ratio decreases from 2.48 at 50 °C to 2.10 at 200 °C. However, it should be pointed out that the O content is calculated based on all the bonding configurations including O−H rather than only Sn−O bonding. The mass density increases with temperature. A compact film with a high mass density of 6.1 g/cm^3 is obtained at 200 °C, approaching the mass density of 6.9−7.0 g/cm^3 for crystalline SnO_2.[39,43,58] The increase in the refractive index n shown in Table 1 is consistent with this increase in density.

3.1.2. Electrical Properties. Electrical properties are of key importance for SnO_2 as an electron transport material. Consequently, carrier density N_e, Hall mobility μ_H, and resistivity ρ of the SnO_2 films have been determined from Hall measurements. The data are summarized in Table 2. The film deposited at 50 °C was not measurable because of a too high electrical resistivity. SnO_2 films with a high electrical resistivity which cannot be measured by Hall measurement have been reported in the literature.[45,47,48] The n-type conductivity is significantly improved at higher deposition temperatures of 150 and 200 °C. It is notable that primarily, the mobility is significantly enhanced when increasing the

Table 1. Mass Density and Relative Elemental Concentration Obtained from RBS/ERD and XPS Measurements for SnO₂ Films Deposited at Different Substrate Temperatures[a]

temp. [°C]	cycles	SE (ex situ)		RBS/ERD								XPS	
		thick. [nm]	n@1.96 eV	mass density [g/cm³]	H [10^{15} at./cm²]	O [10^{15} at./cm²]	Sn [10^{15} at./cm²]	H [at. %]	O [at. %]	Sn [at. %]	O/Sn	C [at. %]	N [at. %]
50	260	31	1.75 ± 0.02	4.10	42.9	120.2	48.7	20	57	23	2.85	6 ± 0.4	6 ± 0.6
100	295	29	1.86 ± 0.02	5.16	28.2	131.2	58.7	13	60	27	2.22	3 ± 0.4	2 ± 0.8
150	270	29	1.95 ± 0.02	5.17	15.0	119.6	59.5	8	61	31	1.97	1 ± 0.5	1 ± 0.4
200	295	36	2.00 ± 0.02	6.14	10.8	182.9	88.9	4	65	31	2.10	0[b]	0[b]

[a]Film thicknesses and refractive indices from SE measurements are also included. The relative errors in atomic percentages of Sn, O, and H measured by RBS/ERD are 2, 4, and 7%, respectively. Detection sensitivities for C and N of these samples are 20 × 10¹⁵ at./cm² and 15 × 10¹⁵ at./cm², respectively. The standard deviations for C and N contamination measured by XPS are calculated based on 3–5 samples for each temperature. [b]Negligible. See Figure S3.

Table 2. Electrical Properties of SnO₂ Films Deposited at Various Substrate Temperatures as Obtained from Hall Measurements[a]

temp. [°C]	thickness [nm]	carrier density N_e [×10^{19} cm⁻³]	mobility μ_H [cm²/V s]	resistivity ρ [mΩ cm]
50	33 ± 0.6			
100	30 ± 0.4			
150	32 ± 0.1	6.5 ± 1.0	9 ± 1	10.7 ± 0.3
200	18 ± 0.2	9.6 ± 0.5	36 ± 1	1.8 ± 0.03
200	33 ± 0.5	8.4 ± 0.2	35 ± 1	2.1 ± 0.05

[a]The layers deposited at 50 and 100 °C are not measurable because of a too large electrical resistivity. Five samples were measured in each series, and standard deviations are included.

deposition temperature from 150 to 200 °C, probably because of an enhanced mass density and thus an enhanced electrical continuity in the lateral direction at a higher deposition temperature (see enhanced mass density in Table 1), in combination with reduced impurity levels as confirmed by XPS analysis (Table 1 and Figure S3). The mobility reported in this work is significantly higher compared to that previously reported for atomic-layer-deposited SnO₂ films deposited at a similar temperature,[45,47,59] and is comparable to that of films deposited at a higher temperature of 250 °C containing a significant crystalline fraction.[47] Regarding the origin of the n-type conductivity, density functional theory calculations have suggested that both oxygen vacancies (V₀) and Sn interstitials (Snᵢ) in the lattice structure could act as shallow donors.[60] Also, hydrogen atoms incorporated on substitutional oxygen sites were suggested to form shallow donors for the n-type conductivity of SnO₂.[61] In the present work, we believe both oxygen vacancies and H shallow dopants contribute to the n-type conductivity of atomic-layer-deposited SnO₂. Despite a much higher H concentration measured for the 50 °C SnO₂ with respect to the 200 °C SnO₂ (Table 1), H atoms are primarily present as O−H and C−H bonds, therefore they are inactive for doping.

3.1.3. Structural and Morphological Properties. To obtain information on the crystallinity of SnO₂ deposited at different deposition temperatures, the films were evaluated by grazing-incidence XRD. Figure 2 shows the XRD patterns of the SnO₂ deposited on ITO glass at 50 and 200 °C. The 50 °C SnO₂ is amorphous, while the film deposited at 200 °C exhibits SnO₂ crystalline peaks of (110) and (200) at 26.6° and 38.3°,
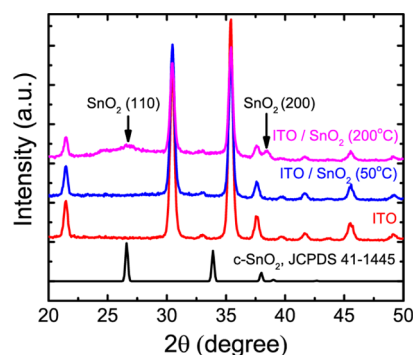
Figure 2. Grazing-incidence XRD patterns of 30 nm thick SnO₂ thin films prepared by ALD at deposition temperatures of 50 and 200 °C on ITO glass substrates. XRD patterns of crystalline SnO₂ (JCPDS 41-1445) and of the ITO glass substrate are included as references.
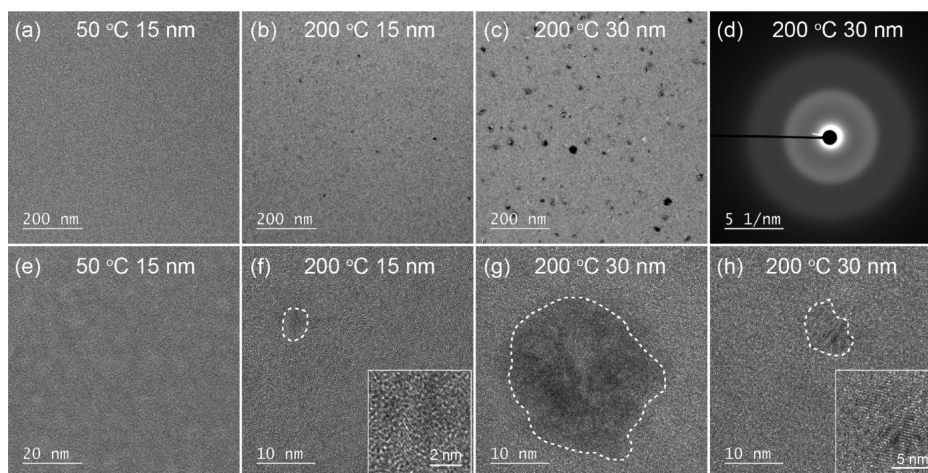
Figure 3. Top-view TEM images of SnO$_2$ films deposited on TEM windows consisting of a SiN membrane coated with a ~5 nm thick atomic-layer-deposited SiO$_2$ layer. Deposition temperature and film thickness: (a) 50 °C, 30 nm, (b) 200 °C, 15 nm, and (c) 200 °C, 30 nm. (e,f) are the high-magnification images of (a,b), respectively. (g,h) are the high-magnification images of (c) showing crystallites of different sizes in an amorphous matrix. The SnO$_2$ crystallites are indicated by the dashed lines. Insets in (f,h) are the enlarged views of the tiny crystallites. (d) Electron diffraction pattern of (c).
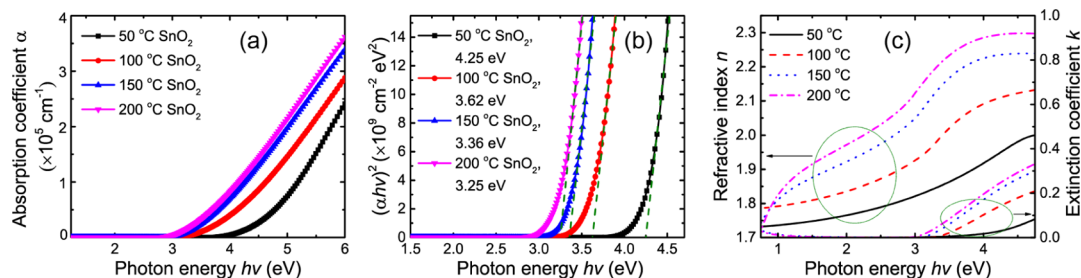
Figure 4. Optical properties of ~30 nm thick SnO$_2$ films prepared by ALD at substrate temperatures of 50, 100, 150 and 200 °C. (a) Absorption coefficient α. (b) Corresponding Tauc plots to determine the optical band gaps of the films, with the values shown in the legend. (c) Refractive index (n) and extinction coefficient (k) as a function of photon energy $h\nu$ for SnO$_2$ films deposited on polished c-Si wafers.

respectively. The broadening of the (110) peak can be attributed to a very small size of the crystallites, which was further examined by TEM. The low intensity of these two peaks can be explained by the low crystalline fraction, as well as the small film thickness of only ~30 nm. A similar crystallinity is found for the SnO$_2$ films deposited at 200 °C on c-Si wafer substrates (Figure S5). The XRD results are in line with those reported for SnO$_2$ films deposited by ALD at comparable deposition temperatures using the TDMASn precursor, though different oxidation sources of hydrogen peroxide,[43,45] water vapor,[46] and ozone[47] were used in their work.

TEM and AFM have been adopted to infer the morphology and grain size of the films. Figure 3 displays the top-view TEM images. No crystallites are identified for the 30 nm thick film deposited at 50 °C (Figure 3a,e). The 15 and 30 nm thick films grown on polished c-Si exhibit a small root-mean-square (rms) roughness of only 0.23 and 0.33 nm, respectively, as measured by AFM (Figure S6). In contrast, nanocrystallites of 4−5 nm in the lateral direction emerge from the amorphous matrix for the 15 nm thick film deposited at 200 °C (the dark phase in Figure 3b, as is also indicated by the dashed line in Figure 3f). These nanocrystallites result in a larger rms of 0.51 nm (Figure S6). Upon increasing the film thickness from 15 to 30 nm at 200 °C, larger crystallites of various sizes (e.g. ~25 nm in Figure 3g and 7−8 nm in Figure 3h) with a higher site density are obtained (Figure 3c), together with a significantly enhanced rms roughness of 1.54 nm. The electron diffraction pattern

shown in Figure 3d indicates that the matrix of the film deposited at 200 °C remains amorphous.

3.1.4. Optical Properties. Optical properties of the films have been characterized by SE and UV−Vis−NIR spectroscopy. Figure 4a compares the absorption coefficients extracted from SE measurements for the SnO$_2$ films, with Figure 4b showing the Tauc band gap values assuming a direct band gap of SnO$_2$.[45,51,62] The optical band gap decreases from 4.25 to 3.25 eV with an increase in the deposition temperature from 50 to 200 °C. Similarly, large optical band gaps in the range of 4.0−4.4 eV have been reported for amorphous SnO$_2$ deposited by ALD below 100 °C, which decreased to slightly below 3 eV upon increasing the deposition temperature to 200 °C, corresponding to an enhanced crystallinity.[45−47] Refractive index (n) and extinction coefficient (k) values are shown in Figure 4c. The SnO$_2$ films are highly transparent in the investigated wavelength range. This is confirmed by the UV−Vis−NIR transmission and reflection spectra shown in Figure S7.

3.2. SnO$_2$/Perovskite Interface Analysis. The interfacial properties [band alignment, work function (WF), etc.] determine the effectiveness of charge extraction and the extent of recombination. To gain insights into these aspects, WF and valence-band-maximum values of SnO$_2$ and perovskite films have been measured by UPS. Figure 5a,b shows the UPS spectra of the SnO$_2$ films deposited on c-Si with a native oxide layer. A WF of 4.11 eV and an ionization energy (IE) of 7.95
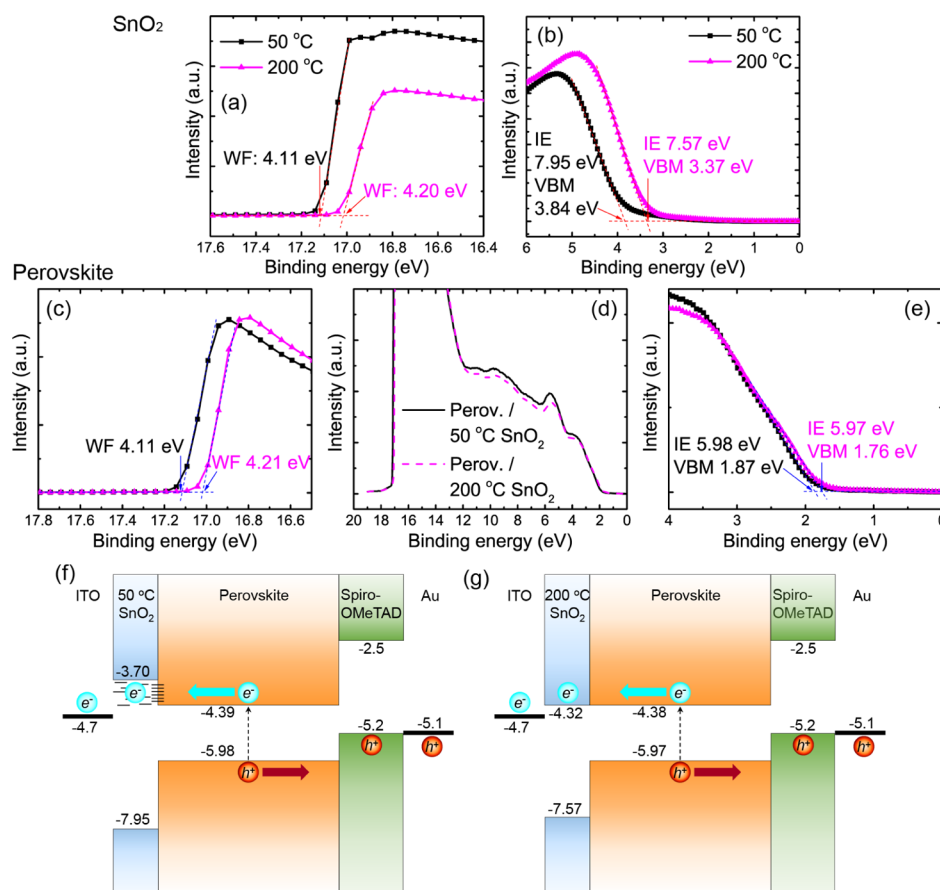
Figure 5. UPS spectra of 15 nm thick SnO_2 films deposited on c-Si at 50 and 200 °C, and of ~500 nm thick $Cs_{0.05}(MA_{0.17}FA_{0.83})_{0.95}Pb(I_{2.7}Br_{0.3})$ perovskite films deposited on the SnO_2 layers. The intersections of the linear extrapolation of the spectra onsets with the background indicate the WF values for the SnO_2 (a) and for the perovskite (c), and the VBM for the SnO_2 (b) and the perovskite (e). IE values of the SnO_2 and the perovskite are also indicated on the labels. (d) Full-range UPS spectra of the perovskite films atop the SnO_2 layers. (f,g) Energy levels (in eV) of the applied layers in the $Cs_{0.05}(MA_{0.17}FA_{0.83})_{0.95}Pb(I_{2.7}Br_{0.3})$ PSCs using atomic-layer-deposited SnO_2 films deposited at 50 (f) and 200 °C (g) as the ETLs. The arrows indicate the moving directions of holes (h^+) and electrons (e^-).

eV are measured for the 50 °C SnO_2. Comparable values are measured for the SnO_2 film grown on an ITO glass substrate (Figure S8). A CBM of 3.70 eV is calculated using CBM = IE − E_g, where E_g is the Tauc band gap of 4.25 eV. For the 200 °C SnO_2, a WF of 4.2 eV, a shallower VB edge of 7.57 eV is found resulting in a deeper CBM of 4.32 eV using the Tauc E_g of 3.25 eV. A similar ~0.5 eV downward shift of CBM has been reported upon crystallization of as-deposited amorphous SnO_2 prepared at 118 °C.[48] The WF values obtained in this work fall in the range of 4.1−4.6 eV previously reported for SnO_2 films fabricated by ALD[24,25,50] and by solution processing.[68] The downward shift of CBM and upward shift of VBM for the 200 °C SnO_2 could have a detrimental impact on the quasi-Fermi splitting in the perovskite, and on the hole blocking ability,[33,48] which could result in a lower V_{oc} of the PSCs.

For both the 50 and 200 °C SnO_2, no obvious gap states are visible in the VB spectra of the SnO_2 layers (Figure 5b). Note that the UPS VB spectra are similar to those measured by XPS (Figure S4a), and the VBM values extracted from the two different characterization methods are also fairly comparable.

Figure 5c,d depicts the UPS VB spectra of the perovskite layers. To calculate the CBM of $Cs_{0.05}(MA_{0.17}FA_{0.83})_{0.95}Pb(I_{2.7}Br_{0.3})$ perovskite, an E_g of 1.59 eV is used, which was measured by PL. Similar IE values are determined for the

perovskites grown on SnO_2 deposited at either 50 or 200 °C. These IE values of ~6 eV of our triple cation perovskites are in a fairly comparable range with respect to those reported for mixed-cation perovskites.[25,26] It has previously been reported that IE values vary in a broad range of 5.67−6.40 eV for $CH_3NH_3PbI_3$ depending on the preparation conditions and stoichiometry of the perovskite, that is, both excess PbI_2 ($CH_3NH_3^+$-deficient and Pb^{2+}-rich) and mixed halide cations increase the IE values of the perovskite.[63,64] The PbI_2 phase is indeed present in our freshly fabricated perovskite films (see Figure S10), which is mainly from the unreacted excess PbI_2 in the precursor solution.

Figure 5f,g depicts the energy-level diagrams of the devices. A notable 0.69 eV CBM mismatch is present at the interface between the 50 °C SnO_2 and the perovskite, whereas an excellent CBM alignment is demonstrated for the 200 °C SnO_2. Simulated band bending diagrams for the devices in dark equilibrium are provided in Figure S14. Surprisingly, this energy-level mismatch does not cause a severe deterioration in the initial cell performance, as will be shown in the next section. In addition, because of the SnO_2 thickness of 15 nm, tunneling of the electrons is unlikely to occur. Therefore, a reasonable scenario is that some shallow defects could play a role in assisting the electron extraction across the $SnO_2/$ perovskite interface. At the other side of the band gap,

sufficiently higher energy barriers at the VBM to block hole transport are demonstrated for both types of SnO_2.

As a comparison of electron extraction at the interfaces between the perovskite and the two different SnO_2 ETLs, steady-state and TRPL measurements are shown in Figure 6a.
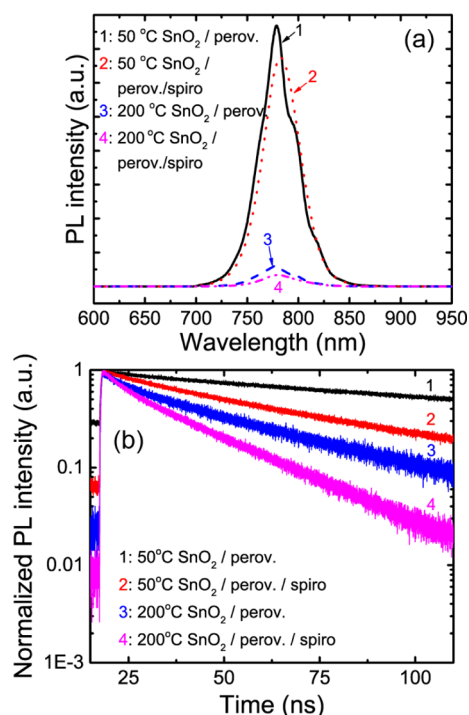
Figure 6. (a) Steady-state and (b) TRPL spectra of complete perovskite cells with a configuration of glass/ITO/SnO_2/perovskite/spiro-OMeTAD/Au (labeled as SnO_2/perov./spiro) and of semicells of glass/ITO/SnO_2/perovskite (labeled as SnO_2/perov.). The atomic-layer-deposited SnO_2 layers were deposited at either 50 or 200 °C.

The perovskite absorbers exhibit emission peaks centered at around 780 nm, corresponding to a band gap of 1.59 eV. This band gap value is confirmed by Fourier transform photocurrent spectroscopy (FTPS) as shown in Figure S9 (1.57 eV). Asymmetric PL peaks are recorded for the bare perovskites on top of both types of SnO_2, though the asymmetricity is less visible for the perovskite on the 200 °C SnO_2 because of the lower peak intensity. This asymmetricity is indicative of phase separation during the PL measurements in air. In contrast, symmetric PL peaks (Figure 6a) are observed when the perovskites are encapsulated with the spiro-OMeTAD/Au layer stack, indicating negligible phase separation in the complete devices based on either 50 or 200 °C SnO_2.

A remarkable PL intensity quenching (Figure 6a) and a faster decay of the charge lifetime (Figure 6b) are seen for the perovskite deposited on the 200 °C SnO_2 compared to the counterpart grown on the 50 °C SnO_2, with or without a hole transport layer of spiro-OMeTAD atop the SnO_2/perovskite layer stack. It is widely accepted that the quenching and the faster decay of the carrier lifetime are indications of a more efficient charge extraction from the perovskite to the charge transport layer(s), considering comparable bulk perovskites.[33,54,65] However, it should be pointed out that the PL signal is influenced by both interface recombination and charge extraction. It is not straightforward to distinguish both

contributions to the PL signal. Considering that the 200 °C SnO_2 possesses a much higher electron mobility and a much better conduction band match with the perovskite, we believe that the PL quenching is indicative of a faster charge extraction at the 200 °C SnO_2/perovskite interface.

3.3. SnO_2 as an ETL in PSCs. To correlate material properties of SnO_2 with the performance of PSCs, SnO_2 films deposited at 50 and 200 °C have been implemented as ETLs in planar $Cs_{0.05}(MA_{0.17}FA_{0.83})_{0.95}Pb(I_{2.7}Br_{0.3})$ PSCs. Figure 7a
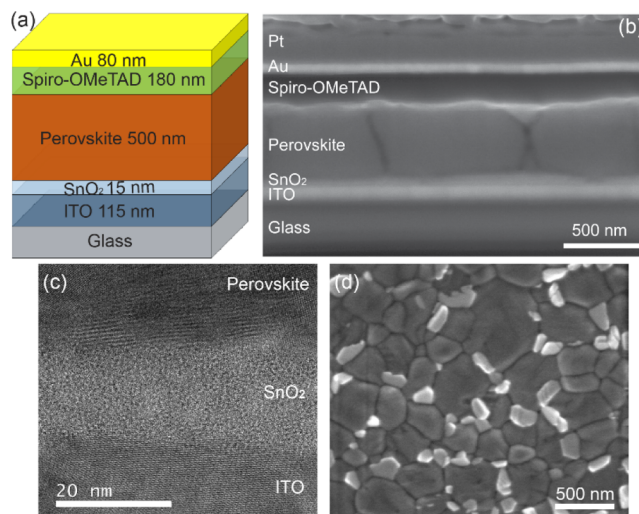
Figure 7. (a) Schematic diagram of the solar cell design. (b) Cross-sectional SEM image of the complete cell using SnO_2 deposited at 50 °C as the ETL. (c) TEM image of the ITO/SnO_2/perovskite interfaces. (d) Top-view SEM image of the perovskite grains grown on the 50 °C SnO_2. The gray phases are PbI_2.

depicts a schematic diagram of the cell design. An SEM cross-sectional image of the complete cell and a top-view image of the perovskite grains grown on the SnO_2 layer deposited at 50 °C are shown in Figure 7b,d, respectively. Large perovskite grains of various sizes are visible in the SEM images, indicating a good crystallization quality of the perovskite grown on the SnO_2 film. Figure 7c presents a high-resolution cross-sectional TEM image displaying the ITO/SnO_2/perovskite interfaces, from which an amorphous SnO_2 layer of 15−16 nm thick is distinguishable from the adjacent polycrystalline ITO and perovskite layers. A lower magnification cross-sectional TEM image of the complete cell is shown in Figure S11, in which a conformal SnO_2 layer with excellent thickness homogeneity atop the ITO substrate is clearly visible. Though a detailed cross-sectional TEM analysis is not available for the perovskite grown on the 200 °C SnO_2, a comparison between the perovskites grown on both types of SnO_2 is performed via top-view SEM imaging and XRD. On the basis of these observations, we conclude that a fairly similar morphology and an identical structure are obtained for the perovskites grown on the different SnO_2 layers (Figure S10).

In order to further study the SnO_2/perovskite interface, a more detailed high-angle annular dark field (HAADF) scanning TEM image with associated EDX elemental mappings and the line scan profile is acquired on several SnO_2/perovskite interface regions. The results are shown in Figures 8 and S12. A fairly homogeneous distribution of the elements is found in the interface region of the perovskite. No PbI_2 interfacial layer at the SnO_2/perovskite interface is
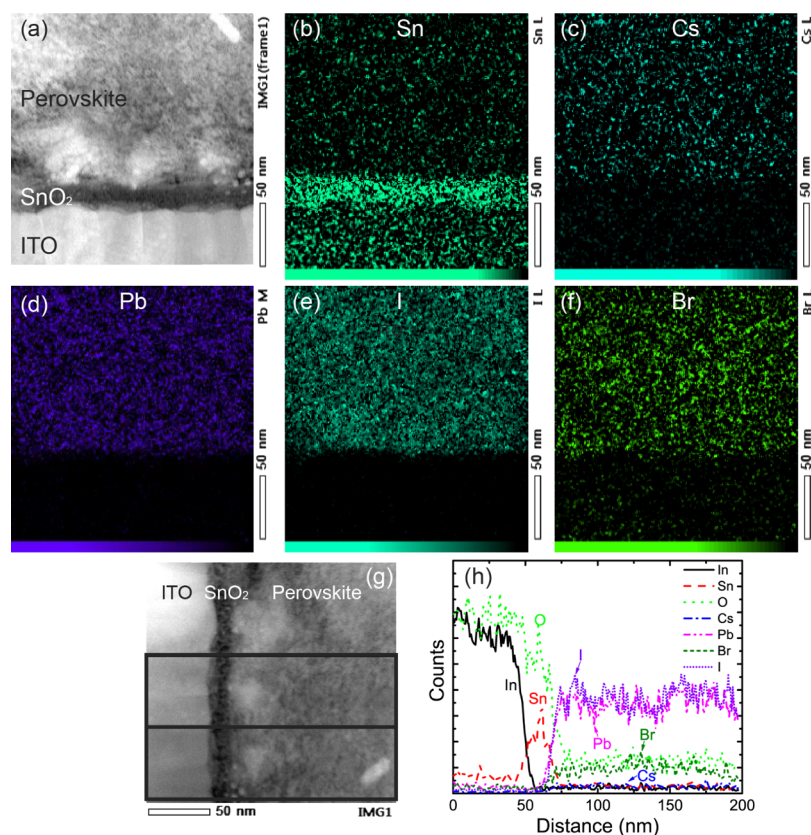
Figure 8. HAADF scanning TEM cross-sectional image of the ITO/SnO$_2$/perovskite interfaces (a), with associated EDX individual elemental maps (b−f). (h) Compositional profiles at the interface, constructed from a two-dimensional EDX map by averaging over the area indicated by the black box in the image (g).
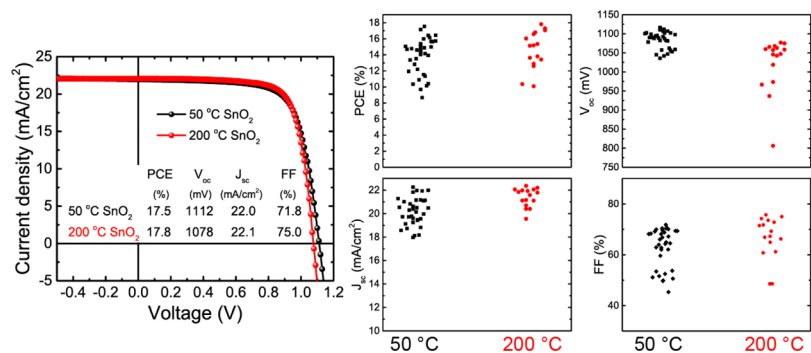
Figure 9. Reverse J−V scans (scan rate: 200 mV/s, stepwise: 10 mV) for the champion PSCs using 15 nm thick atomic-layer-deposited SnO$_2$ films deposited at 50 or 200 °C as the ETLs. The inset shows the extracted PV characteristics. Statistics on PCE, V_{oc}, J_{sc}, and FF extracted from reverse J−V scans are also included.

characterized by TEM and EDX, whereas its presence between atomic-layer-deposited SnO$_2$ and MAPbI$_3$ layers was reported in the literature.[50]

The performance of the PSCs has been characterized via J−V measurements under AM1.5G illumination. Figure 9 shows plots of the reverse J−V scans of the best performing PSCs. Comparable PCEs of 17.5 and 17.8% have been achieved for the champion cells using 50 and 200 °C SnO$_2$. Statistics on PCE, V_{oc}, J_{sc}, and FF of the devices are also present in Figure 9. A total number of 35 and 16 PSCs from three batches using 50 and 200 °C SnO$_2$ ETLs have been tested for the statistics, respectively. We notice a scattering of the J−V data. As the atomic-layer-deposited SnO$_2$ is deposited under a well-controlled condition with excellent reproducibility, the data

fluctuation is mainly ascribed to the variation on the nucleation and growth of the perovskite on the SnO$_2$. The average cell characteristics from backward J−V scans of the top 10 devices of each group are listed in Table 3. The cells with 50 °C SnO$_2$ perform on average slightly better in V_{oc} but slightly worse in

Table 3. Average J−V Characteristics with Standard Deviations from the Top 10 Devices Using Either 50 or 200 °C SnO$_2$

sample	J_{sc} [mA/cm^2]	V_{oc} [mV]	FF [%]	PCE [%]
50 °C SnO$_2$	21.4 ± 0.6	1086 ± 25	70 ± 2	16.2 ± 0.7
200 °C SnO$_2$	21.3 ± 0.9	1061 ± 11	71 ± 4	16.1 ± 1

FF with respect to the cells adopting the 200 °C SnO$_2$. The lower FF values are mainly attributed to a much higher series resistance for the 50 °C SnO$_2$, as indicated by the Hall measurements shown in Table 2. The higher V_{oc} could be explained by the upward shift of CBM and downward shift of VBM for the 50 °C SnO$_2$ (Figure 5), which could lead to a broader quasi-Fermi splitting in the perovskite. In addition, it was found by Lee et al. that residual TDMASn precursors can passivate SnO$_2$ deposited at 100 °C by ALD.[54] In the present work, the SnO$_2$ film deposited at 50 °C contains a significant amount of C and N impurities as well as OH groups from an incomplete reaction of the precursors as confirmed by XPS spectra (Figure S3). The similar self-passivation effect from the residual TDMASn precursors might also exist in the 50 °C SnO$_2$. This passivation could reduce recombination at the SnO$_2$/perovskite interface, which is consistent with the larger V_{oc} for the devices using the 50 °C SnO$_2$. Furthermore, this speculation agrees with the higher PL signal and the longer TRPL lifetime for the perovskite grown on the 50 °C SnO$_2$ (Figure 6).

The J–V characteristics of our devices are comparable to those of state-of-the-art planar n–i–p PSCs based on atomic-layer-deposited SnO$_2$ ETLs. For instance, Lee et al. reported similar J–V parameters of 22.59 ± 0.15 mA/cm^2, 1.07 ± 0.04 V, 0.73 ± 0.03, and (17.75 ± 0.62)% using a cell configuration of FTO/SnO$_2$/FAMAPb(I,Br)$_3$/PTAA/Au.[54] By applying a compact TiO$_2$ layer underneath the SnO$_2$ forming a bilayer ETL, the cell performance was further improved to 22.68 ± 0.30 mA/cm^2, 1.13 ± 0.01 V, 0.78 ± 0.01, and 19.83 ± 0.02%. The enhancement was mainly attributed to a better hole blocking ability, thanks to the underlying compact TiO$_2$ layer. Wang et al. reported 21.17 mA/cm^2, 1.074 V, 75.48, and 17.16% for their PSCs using a configuration of FTO/SnO$_2$/MAPbI$_3$/spiro-OMeTAD/Au, with the SnO$_2$ deposited at 100 °C by plasma-enhanced ALD. Inserting a C$_{60}$-self-assembled monolayer passivation at the SnO$_2$/perovskite interface improved the PCE to 18.21% because of increased V_{oc} and FF.[49] These works point out that there is still room for performance gain in the present work via optimization of the SnO$_2$/perovskite interface.

Hysteresis is present between the forward and reverse J–V scans for both types of PSCs, as shown in Figure S13 and Table S1. Halide ion migration and unbalanced charge extraction are generally believed to be the most probable reasons among several potential causes for hysteresis in J–V characteristics.[3,66−68] An imperfect interfacial structure could cause a charge accumulation at the interface, which consequently leads to hysteresis in the J–V scans.[25,66] Hysteresis is commonly seen in other works applying SnO$_2$ as ETLs prepared by either ALD[49−51,54] or solution process methods in planar PSCs.[31,68,69] It was reported that a low electron mobility of SnO$_2$ prepared by ALD at 100 °C is partly responsible for the hysteresis of PSCs.[51] However, in our study, the hysteresis is not reduced by applying the 200 °C SnO$_2$ with a high electron mobility of 36.0 cm^2/V s in the PSCs. This observation leads to a hypothesis that hysteresis in the present work can be rather ascribed to halide ion migration near the interface and interface defects instead of bulk properties of both SnO$_2$ and perovskite. Hysteresis is shown in the literature to be quantitatively suppressed by introducing an interfacial defect passivation layer of, for example, fullerene C60 layer,[31,49,51] or [6,6]-phenyl C60 (or C70) butyric acid methyl ester (PCBM) layer,[68] or amorphous SnOCl$_2$.[33] In the

present work, with the insertion of a PC$_{60}$BM layer (purchased from Nano-C) by spin-coating between SnO$_2$ and perovskite, the hysteresis indeed was significantly reduced (Figure S13a,b). Electron extraction could be promoted at this interface, thereby reducing the hysteresis.

In the literature, a so-called stabilized efficiency is typically measured under continuous AM1.5G illumination at the maximum power point (MPP) with a duration in the range of 150−600 s. In the current work, we extended the test duration to 16 h to check the light stability of the PSCs. Markedly, the compact SnO$_2$ deposited at 200 °C results in a reasonably stable cell performance over 16 h measured in a nitrogen filled glovebox, as depicted in Figure 10. Interestingly,
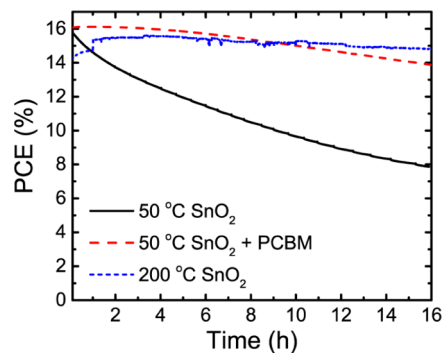
Figure 10. Evolution of PCE measured at the MPP (PCE$_{mpp}$) over 16 h under continuous AM1.5G illumination; 15 nm thick SnO$_2$ layers deposited either at 50 or 200 °C with or without a PCBM layer were used as the ETLs for the cells.

a rise in PCE is observed during the first hour corresponding to increase in both voltage (V_{mpp}) and photocurrent (J_{mpp}) (not shown). Increase in PCE during the first 400 h under MPP tracking is reported in the literature. In that work, an inverted p–i–n architecture with Cs$_{0.17}$FA$_{0.83}$Pb(Br$_{0.17}$I$_{0.83}$)$_3$ perovskite grown on a NiO$_x$ film is employed. They ascribed the PCE rise to the improvement of the NiO$_x$/perovskite interface or the increased perovskite crystallinity.[53] In the present case, we tend to believe a potential improvement of the SnO$_2$/perovskite interface under illumination could be responsible for the rise in PCE. In contrast, the PCE of the counterpart cell using the 50 °C SnO$_2$ decreases by approximately 50% after 16 h because of a decrease in both photocurrent and voltage. This phenomenon was reproduced in other identical devices. However, the decrease in PCE is significantly reduced when applying a PCBM interfacial layer between the 50 °C SnO$_2$ and the perovskite. These observations lead to a conclusion that the 50 °C SnO$_2$/perovskite interface suffers from a light instability issue. We speculate the potential reasons for the degradation including photoactivated defects and band alignment variation upon illumination, which lead to charge accumulation and recombination at the ETL/perovskite interface. The 50 °C SnO$_2$ exhibits conduction band offset and lower charge mobility with respect to the 200 °C SnO$_2$, as the latter owns an excellent conduction band alignment with the perovskite and a much higher electron mobility. The PCBM interlayer could result in a more favorable band alignment for faster charge extraction and a reduced interfacial recombination upon illumination, which explain the gentle degradation under light soaking. Pérez-del-Rey et al. reported similar findings by inserting a thin (<10 nm) interlayer of C$_{60}$ at the TiO$_2$/

MAPbI$_3$ interface.[70] Interfacial properties including leakage current, interfacial recombination, and band alignment are improved after a bias/ultraviolet light activation with the presence of this interlayer. Nevertheless, in the current work, the exact mechanisms for the PCE degradation are not fully understood. Further study of the mechanisms for stability under a longer light soaking is thus required.

4. CONCLUSIONS

In summary, bulk (chemical, structural, electrical, and optical) properties and interfacial properties of atomic-layer-deposited SnO$_2$ as an electron transport material for PSCs have been studied. Highly transparent amorphous SnO$_2$ films are prepared in a temperature range of 50−200 °C by plasma-assisted atomic layer deposition. The SnO$_2$ films possess deep VBs for hole blocking at the SnO$_2$/perovskite interface. An excellent conduction band alignment is demonstrated between the 200 °C SnO$_2$ and the perovskite. In contrast, a conduction band offset is present between the 50 °C SnO$_2$ and the perovskite. However, electron transport at this interface is not blocked by this energy offset when keeping the ETL thin at 15 nm. Comparable initial efficiencies are demonstrated for the PSCs using either 50 or 200 °C SnO$_2$ as the ETL. The electrically conductive SnO$_2$ with a high electron mobility deposited at 200 °C results in on average a slightly higher FF but lower V_{oc} for the PSCs with respect to those using the resistive SnO$_2$ deposited at 50 °C. Current−voltage hysteresis is present in the PSCs regardless of whether resistive or conductive SnO$_2$ is employed. The introduction of a PCBM interfacial layer between the SnO$_2$ and the perovskite significantly reduces this hysteresis. Regarding light stability, the SnO$_2$ deposited at 200 °C contributes to a more stable cell performance over 16 h under continuous AM1.5G illumination. In contrast, the efficiency decreases by approximately 50% for the counterpart device using the 50 °C SnO$_2$. We believe the SnO$_2$/perovskite interface is critical for both initial performance and long-term light stability. Further investigation of defects and chemical bonding at the SnO$_2$/perovskite interface and their role in device performance is therefore of key importance to promote the application of atomic-layer-deposited SnO$_2$ as the ETL in planar PSCs.

ASSOCIATED CONTENT

S Supporting Information

The Supporting Information is available free of charge on the ACS Publications website at DOI: 10.1021/acsami.8b09515.

Schematics for the ALD reactor and the ALD recipe; XPS, XRD spectra, and AFM images for the SnO$_2$ films deposited at 50, 100, 150, and 200 °C; TEM images for the SnO$_2$ films deposited at 50 and 200 °C; transmission and reflection spectra for the SnO$_2$ films deposited on ITO glass substrates; UPS spectra for the SnO$_2$ films deposited on c-Si (100) wafers and on ITO glass substrates; FTPS, XPS, XRD spectra, and SEM images for the perovskites grown on the SnO$_2$ films; TEM cross-sectional image of the complete perovskite cell with associated EDX individual elemental maps; solar cell characteristics extracted from reverse and forward scans at scan rates of 20, 200, and 2000 mV/s for the PSCs using SnO$_2$ and SnO$_2$/PCBM bilayer as the ETL; procedures for simulations using a solar cell capacitance simulator in one-dimensional (SCAPS-1D) software;

and simulated band bending diagrams for the PSCs (PDF)

AUTHOR INFORMATION

Corresponding Author
*E-mail: M.Creatore@tue.nl.
ORCID
Yinghuan Kuang: 0000-0002-1564-842X
Saurabh Karwal: 0000-0001-7959-1138
Lachlan E. Black: 0000-0002-9807-8433
Wilhelmus M.M. Kessels: 0000-0002-7630-8226
Present Address
⊥Thin-film photovoltaics group, imec, EnergyVille 2, Thor Park 8320, 3600 Genk, Belgium.
Notes
The authors declare no competing financial interest.

ACKNOWLEDGMENTS

REFERENCES

(1) Kojima, A.; Teshima, K.; Shirai, Y.; Miyasaka, T. Organometal Halide Perovskites as Visible-Light Sensitizers for Photovoltaic Cells. *J. Am. Chem. Soc.* **2009**, *131*, 6050−6051.

(2) https://www.nrel.gov/pv/assets/images/efficiency-chart.png (accessed in August, 2018).

(3) Park, N.-G.; Grätzel, M.; Miyasaka, T.; Zhu, K.; Emery, K. Towards Stable and Commercially Available Perovskite Solar Cells. *Nat. Energy* **2016**, *1*, 16152.

(4) De Wolf, S.; Holovsky, J.; Moon, S.-J.; Löper, P.; Niesen, B.; Ledinsky, M.; Haug, F.-J.; Yum, J.-H.; Ballif, C. Organometallic Halide Perovskites: Sharp Optical Absorption Edge and Its Relation to Photovoltaic Performance. *J. Phys. Chem. Lett.* **2014**, *5*, 1035−1039.

(5) Frost, J. M.; Butler, K. T.; Brivio, F.; Hendon, C. H.; van Schilfgaarde, M.; Walsh, A. Atomistic Origins of High-Performance in Hybrid Halide Perovskite Solar Cells. *Nano Lett.* **2014**, *14*, 2584−2590.

(6) Yang, J.; Siempelkamp, B. D.; Liu, D.; Kelly, T. L. Investigation of CH$_3$NH$_3$PbI$_3$ Degradation Rates and Mechanisms in Controlled Humidity Environments Using in Situ Techniques. *ACS Nano* **2015**, *9*, 1955−1963.

(7) Christians, J. A.; Herrera, P. A. M.; Kamat, P. V. Transformation of the Excited State and Photovoltaic Efficiency of CH$_3$NH$_3$PbI$_3$ Perovskite upon Controlled Exposure to Humidified Air. *J. Am. Chem. Soc.* **2015**, *137*, 1530−1538.

(8) Han, Y.; Meyer, S.; Dkhissi, Y.; Weber, K.; Pringle, J. M.; Bach, U.; Spiccia, L.; Cheng, Y.-B. Degradation Observations of

Encapsulated Planar CH$_3$NH$_3$PbI$_3$ Perovskite Solar Cells at High Temperatures and Humidity. *J. Mater. Chem. A* **2015**, *3*, 8139−8147.

(9) Conings, B.; Drijkoningen, J.; Gauquelin, N.; Babayigit, A.; D'Haen, J.; D'Olieslaeger, L.; Ethirajan, A.; Verbeeck, J.; Manca, J.; Mosconi, E.; De Angelis, F.; Boyen, H.-G. Intrinsic Thermal Instability of Methylammonium Lead Trihalide Perovskite. *Adv. Energy Mater.* **2015**, *5*, 1500477.

(10) Philippe, B.; Park, B.-W.; Lindblad, R.; Oscarsson, J.; Ahmadi, S.; Johansson, E. M. J.; Rensmo, H. Chemical and Electronic Structure Characterization of Lead Halide Perovskites and Stability Behavior under Different Exposures-A Photoelectron Spectroscopy Investigation. *Chem. Mater.* **2015**, *27*, 1720−1731.

(11) Supasai, T.; Rujisamphan, N.; Ullrich, K.; Chemseddine, A.; Dittrich, T. Formation of a Passivating CH$_3$NH$_3$PbI$_3$/PbI$_2$ Interface during Moderate Heating of CH$_3$NH$_3$PbI$_3$ layers. *Appl. Phys. Lett.* **2013**, *103*, 183906.

(12) Divitini, G.; Cacovich, S.; Matteocci, F.; Cinà, L.; Di Carlo, A.; Ducati, C. In Situ Observation of Heat-Induced Degradation of Perovskite Solar Cells. *Nat. Energy* **2016**, *1*, 15012.

(13) Misra, R. K.; Aharon, S.; Li, B.; Mogilyansky, D.; Visoly-Fisher, I.; Etgar, L.; Katz, E. A. Temperature- and Component-Dependent Degradation of Perovskite Photovoltaic Materials under Concentrated Sunlight. *J. Phys. Chem. Lett.* **2015**, *6*, 326−330.

(14) Jacobsson, T. J.; Schwan, L. J.; Ottosson, M.; Hagfeldt, A.; Edvinsson, T. Determination of Thermal Expansion Coefficients and Locating the Temperature-Induced Phase Transition in Methylammonium Lead Perovskites Using X-ray Diffraction. *Inorg. Chem.* **2015**, *54*, 10678−10685.

(15) Stoumpos, C. C.; Malliakas, C. D.; Kanatzidis, M. G. Semiconducting Tin and Lead Iodide Perovskites with Organic Cations: Phase Transitions, High Mobilities, and Near-Infrared Photoluminescent Properties. *Inorg. Chem.* **2013**, *52*, 9019−9038.

(16) deQuilettes, D. W.; Zhang, W.; Burlakov, V. M.; Graham, D. J.; Leijtens, T.; Osherov, A.; Bulović, V.; Snaith, H. J.; Ginger, D. S.; Stranks, S. D. Photo-Induced Halide Redistribution in Organic-Inorganic Perovskite Films. *Nat. Commun.* **2016**, *7*, 11683.

(17) Cacovich, S.; Ciná, L.; Matteocci, F.; Divitini, G.; Midgley, P. A.; Di Carlo, A.; Ducati, C. Gold and Iodine Diffusion in Large Area Perovskite Solar Cells under Illumination. *Nanoscale* **2017**, *9*, 4700−4706.

(18) Deng, Y.; Xiao, Z.; Huang, J. Light-Induced Self-Poling Effect on Organometal Trihalide Perovskite Solar Cells for Increased Device Efficiency and Stability. *Adv. Energy Mater.* **2015**, *5*, 1500721.

(19) Saliba, M.; Matsui, T.; Seo, J.-Y.; Domanski, K.; Correa-Baena, J.-P.; Nazeeruddin, M. K.; Zakeeruddin, S. M.; Tress, W.; Abate, A.; Hagfeldt, A.; Grätzel, M. Cesium-containing Triple Cation Perovskite Solar Cells: Improved Stability, Reproducibility and High Efficiency. *Energy Environ. Sci.* **2016**, *9*, 1989−1997.

(20) Saliba, M.; Matsui, T.; Domanski, K.; Seo, J.-Y.; Ummadisingu, A.; Zakeeruddin, S. M.; Correa-Baena, J.-P.; Tress, W. R.; Abate, A.; Hagfeldt, A.; Gratzel, M. Incorporation of Rubidium Cations into Perovskite Solar Cells Improves Photovoltaic Performance. *Science* **2016**, *354*, 206−209.

(21) Grätzel, M. Dye-Sensitized Solar Cells. *J. Photochem. Photobiol., C* **2003**, *4*, 145−153.

(22) O'Regan, B.; Grätzel, M. High-Efficiency Solar-Cell Based on Dye-Sensitized Colloidal TiO$_2$ Films. *Nature* **1991**, *353*, 737−740.

(23) Leijtens, T.; Eperon, G. E.; Pathak, S.; Abate, A.; Lee, M. M.; Snaith, H. J. Overcoming Ultraviolet Light Instability of Sensitized TiO$_2$ with Meso-superstructured Organometal Tri-halide Perovskite Solar Cells. *Nat. Commun.* **2013**, *4*, 2885.

(24) Trost, S.; Behrendt, A.; Becker, T.; Polywka, A.; Görrn, P.; Riedl, T. Tin Oxide (SnO$_x$) as Universal "Light-Soaking" Free Electron Extraction Material for Organic Solar Cells. *Adv. Energy Mater.* **2015**, *5*, 1500277.

(25) Baena, J. P. C.; Steier, L.; Tress, W.; Saliba, M.; Neutzner, S.; Matsui, T.; Giordano, F.; Jacobsson, T. J.; Kandada, A. R. S.; Zakeeruddin, S. M.; Petrozza, A.; Abate, A.; Nazeeruddin, M. K.; Grätzel, M.; Hagfeldt, A. Highly Efficient Planar Perovskite Solar Cells through Band Alignment Engineering. *Energy Environ. Sci.* **2015**, *8*, 2928−2934.

(26) Tan, H.; Jain, A.; Voznyy, O.; Lan, X.; de Arquer, F. P. G.; Fan, J. Z.; Quintero-Bermudez, R.; Yuan, M.; Zhang, B.; Zhao, Y.; Fan, F.; Li, P.; Quan, L. N.; Zhao, Y.; Lu, Z.-H.; Yang, Z.; Hoogland, S.; Sargent, E. H. Efficient and Stable Solution-Processed Planar Perovskite Solar Cells via Contact Passivation. *Science* **2017**, *355*, 722−726.

(27) Li, Y.; Zhu, J.; Huang, Y.; Liu, F.; Lv, M.; Chen, S.; Hu, L.; Tang, J.; Yao, J.; Dai, S. Mesoporous SnO$_2$ nanoparticle Flms as Electron-transporting Material in Perovskite Solar Cells. *RSC Adv.* **2015**, *5*, 28424−28429.

(28) Ke, W.; Fang, G.; Liu, Q.; Xiong, L.; Qin, P.; Tao, H.; Wang, J.; Lei, H.; Li, B.; Wan, J.; Yang, G.; Yan, Y. Low-temperature Solution-processed Tin Oxide as an Alternative Electron Transporting Layer for Efficient Perovskite Solar Cells. *J. Am. Chem. Soc.* **2015**, *137*, 6730−6733.

(29) Song, J.; Zheng, E.; Bian, J.; Wang, X.-F.; Tian, W.; Sanehira, Y.; Miyasaka, T. Low-temperature SnO$_2$-based Eectron Selective Contact for Efficient and Stable Perovskite Solar Cells. *J. Mater. Chem. A* **2015**, *3*, 10837−10844.

(30) Zhu, Z.; Zheng, X.; Bai, Y.; Zhang, T.; Wang, Z.; Xiao, S.; Yang, S. Mesoporous SnO$_2$ Single Crystals as an Effective Electron Collector for Perovskite Solar Cells. *Phys. Chem. Chem. Phys.* **2015**, *17*, 18265−18268.

(31) Zhu, Z.; Bai, Y.; Liu, X.; Chueh, C.-C.; Yang, S.; Jen, A. K.-Y. Enhanced Efficiency and Stability of Inverted Perovskite Solar Cells Using Highly Crystalline SnO$_2$ Nanocrystals as the Robust Electron-Transporting Layer. *Adv. Mater.* **2016**, *28*, 6478−6484.

(32) Rao, H.-S.; Chen, B.-X.; Li, W.-G.; Xu, Y.-F.; Chen, H.-Y.; Kuang, D.-B.; Su, C.-Y. Improving the Extraction of Photogenerated Electrons with SnO$_2$ Nanocolloids for Efficient Planar Perovskite Solar Cells. *Adv. Funct. Mater.* **2015**, *25*, 7200−7207.

(33) Lee, Y.; Paek, S.; Cho, K. T.; Oveisi, E.; Gao, P.; Lee, S.; Park, J.-S.; Zhang, Y.; Humphry-Baker, R.; Asiri, A. M.; Nazeeruddin, M. K. Enhanced Charge Collection with Passivation of the Tin Oxide Layer in Planar Perovskite Solar Cells. *J. Mater. Chem. A* **2017**, *5*, 12729−12734.

(34) George, S. M. Atomic Layer Deposition: An Overview. *Chem. Rev.* **2010**, *110*, 111−131.

(35) Profijt, H. B.; Potts, S. E.; van de Sanden, M. C. M.; Kessels, W. M. M. Plasma-Assisted Atomic Layer Deposition: Basics, Opportunities, and Challenges. *J. Vac. Sci. Technol., A* **2011**, *29*, 050801.

(36) Zardetto, V.; Di Giacomo, F.; Mohammed, M. A.; Lucarelli, G.; Razza, S.; D'Epifanio, A.; Licoccia, S.; Kessels, W. M. M.; Di Carlo, A.; Brown, T. M.; Creatore, M. Opportunities of Atomic Layer Deposition for Perovskite Solar Cells. *ECS Trans.* **2015**, *69*, 15−22.

(37) Zardetto, V.; Williams, B. L.; Perrotta, A.; Di Giacomo, F.; Verheijen, M. A.; Andriessen, R.; Kessels, W. M. M.; Creatore, M. Atomic Layer Deposition for Perovskite Solar Cells: Research Status, Opportunities and Challenges. *Sustainable Energy Fuels* **2017**, *1*, 30−55.

(38) Viirola, H.; Niinistö, L. Controlled Growth of Tin Dioxide Thin Films by Atomic Layer Epitaxy. *Thin Solid Films* **1994**, *249*, 144−149.

(39) Du, X.; Du, Y.; George, S. M. In Situ Examination of Tin Oxide Atomic Layer Deposition Using Quartz Crystal Microbalance and Fourier Transform Infrared Techniques. *J. Vac. Sci. Technol., A* **2005**, *23*, 581−588.

(40) Du, X.; Du, Y.; George, S. M. CO Gas Sensing by Ultrathin Tin Oxide Films Grown by Atomic Layer Deposition Using Transmission FTIR Spectroscopy. *J. Phys. Chem. A* **2008**, *112*, 9211−9219.

(41) Tarre, A.; Rosental, A.; Aidla, A.; Aarik, J.; Sundqvist, J.; Hårsta, A. New Routes to SnO$_2$ Heteroepitaxy. *Vacuum* **2002**, *67*, 571−575.

(42) Sundqvist, J.; Lu, J.; Ottosson, M.; Hårsta, A. Growth of SnO$_2$ Thin Films by Atomic Layer Deposition and Chemical Vapour Deposition: A comparative Study. *Thin Solid Films* **2006**, *514*, 63−68.

(43) Elam, J. W.; Baker, D. A.; Hryn, A. J.; Martinson, A. B. F.; Pellin, M. J.; Hupp, J. T. Atomic Layer Deposition of Tin Oxide Films

Using Tetrakis(dimethylamino) Tin. *J. Vac. Sci. Technol., A* **2008**, *26*, 244−252.

(44) Elam, J. W.; Baker, D. A.; Martinson, A. B. F.; Pellin, M. J.; Hupp, J. T. Atomic Layer Deposition of Indium Tin Oxide Thin Films Using Nonhalogenated Precursors. *J. Phys. Chem. C* **2008**, *112*, 1938−1945.

(45) Choi, D.-W.; Maeng, W. J.; Park, J.-S. The Conducting Tin Oxide Thin Films Deposited via Atomic Layer Deposition using Tetrakis-dimethylamino Tin and Peroxide for Transparent Flexible Electronics. *Appl. Surf. Sci.* **2014**, *313*, 585−590.

(46) Mullings, M. N.; Hägglund, C.; Bent, S. F. Tin Oxide Atomic Layer Deposition from Tetrakis(dimethylamino)tin and Water. *J. Vac. Sci. Technol., A* **2013**, *31*, 061503.

(47) Choi, D.-W.; Park, J.-S. Highly Conductive SnO_2 Thin Films Deposited by Atomic Layer Deposition using Tetrakis-dimethyl-amine-tin Precursor and Ozone Reactant. *Surf. Coat. Technol.* **2014**, *259*, 238−243.

(48) Kavan, L.; Steier, L.; Grätzel, M. Ultrathin Buffer Layers of SnO_2 by Atomic Layer Deposition: Perfect Blocking Function and Thermal Stability. *J. Phys. Chem. C* **2017**, *121*, 342−350.

(49) Wang, C.; Zhao, D.; Grice, C. R.; Liao, W.; Yu, Y.; Cimaroli, A.; Shrestha, N.; Roland, P. J.; Chen, J.; Yu, Z.; Liu, P.; Cheng, N.; Ellingson, R. J.; Zhao, X.; Yan, Y. Low-temperature Plasma-Enhanced Atomic Layer Deposition of Tin Oxide Electron Selective Layers for Highly Efficient Planar Perovskite Solar Cells. *J. Mater. Chem. A* **2016**, *4*, 12080−12087.

(50) Hu, T.; Becker, T.; Pourdavoud, N.; Zhao, J.; Brinkmann, K. O.; Heiderhoff, R.; Gahlmann, T.; Huang, Z.; Olthof, S.; Meerholz, K.; Többens, D.; Cheng, B.; Chen, Y.; Riedl, T. Indium-Free Perovskite Solar Cells Enabled by Impermeable Tin-Oxide Electron Extraction Layers. *Adv. Mater.* **2017**, *29*, 1606656.

(51) Wang, C.; Xiao, C.; Yu, Y.; Zhao, D.; Awni, R. A.; Grice, C. R.; Ghimire, K.; Constantinou, I.; Liao, W.; Cimaroli, A. J.; Liu, P.; Chen, J.; Podraza, N. J.; Jiang, C.-S.; Al-Jassim, M. M.; Zhao, X.; Yan, Y. Understanding and Eliminating Hysteresis for Highly Efficient Planar Perovskite Solar Cells. *Adv. Energy Mater.* **2017**, *7*, 1700414.

(52) Brinkmann, K. O.; Zhao, J.; Pourdavoud, N.; Becker, T.; Hu, T.; Olthof, S.; Meerholz, K.; Hoffmann, L.; Gahlmann, T.; Heiderhoff, R.; Oszajca, M. F.; Luechinger, N. A.; Rogalla, D.; Chen, Y.; Cheng, B.; Riedl, T. Suppressed Decomposition of Organometal Halide Perovskites by Impermeable Electron-extraction Layers in Inverted Solar Cells. *Nat. Commun.* **2017**, *8*, 13938.

(53) Bush, K. A.; Palmstrom, A. F.; Yu, Z. J.; Boccard, M.; Cheacharoen, R.; Mailoa, J. P.; Mcmeekin, D. P.; Hoye, R. L. Z.; Bailie, C. D.; Leijtens, T.; Peters, I. M.; Minichetti, M. C.; Rolston, N.; Prasanna, R.; Sofia, S.; Harwood, D.; Ma, W.; Moghadam, F.; Snaith, H. J.; Buonassisi, T.; Holman, Z. C.; Bent, S. F.; McGehee, M. D. 23.6%-Efficient Monolithic Perovskite/Silicon Tandem Solar Cells with Improved Stability. *Nat. Energy* **2017**, *2*, 17009.

(54) Lee, Y.; Lee, S.; Seo, G.; Paek, S.; Cho, K. T.; Huckaba, A. J.; Calizzi, M.; Choi, D.-W.; Park, J.-S.; Lee, D.; Lee, H. J.; Asiri, A. M.; Nazeeruddin, M. K. Efficient Planar Perovskite Solar Cells Using Passivated Tin Oxide as an Electron Transport Layer. *Adv. Sci.* **2018**, *5*, 1800130.

(55) Hoffmann, L.; Brinkmann, K. O.; Malerczyk, J.; Rogalla, D.; Becker, T.; Theirich, D.; Shutsko, I.; Görrn, P.; Riedl, T. Spatial Atmospheric Pressure Atomic Layer Deposition of Tin Oxide as an Impermeable Electron Extraction Layer for Perovskite Solar Cells with Enhanced Thermal Stability. *ACS Appl. Mater. Interfaces* **2018**, *10*, 6006−6013.

(56) Themlin, J.-M.; Chtaïb, M.; Henrard, L.; Lambin, P.; Darville, J.; Gilles, J.-M. Characterization of Tin Oxides by X-ray-photo-emission Spectroscopy. *Phys. Rev. B: Condens. Matter Mater. Phys.* **1992**, *46*, 2460−2466.

(57) Szuber, J.; Czempik, G.; Larciprete, R.; Koziej, D.; Adamowicz, B. XPS Study of the L-CVD Deposited SnO_2 Thin Films Exposed to Oxygen and Hydrogen. *Thin Solid Films* **2001**, *391*, 198−203.

(58) Batzill, M.; Diebold, U. The Surface and Materials Science of Tin Oxide. *Prog. Surf. Sci.* **2005**, *79*, 47−154.

(59) Lee, D.-K.; Wan, Z.; Bae, J.-S.; Lee, H.-B.-R.; Ahn, J.-H.; Kim, S.-D.; Kim, J.; Kwon, S.-H. Plasma-enhanced Atomic Layer Deposition of SnO_2 Thin Films using $SnCl_4$ and O_2 Plasma. *Mater. Lett.* **2016**, *166*, 163−166.

(60) Kılıç, Ç.; Zunger, A. Origins of Coexistence of Conductivity and Transparency in SnO_2. *Phys. Rev. Lett.* **2002**, *88*, 095501.

(61) Singh, A. K.; Janotti, A.; Scheffler, M.; Van De Walle, C. G. Sources of Electrical Conductivity in SnO_2. *Phys. Rev. Lett.* **2008**, *101*, 055502.

(62) Barbé, J.; Tietze, M. L.; Neophytou, M.; Murali, B.; Alarousu, E.; El Labban, A.; Abulikemu, M.; Yue, W.; Mohammed, O. F.; McCulloch, I.; Amassian, A.; Del Gobbo, S. Amorphous Tin Oxide as a Low-Temperature-Processed Electron-Transport Layer for Organic and Hybrid Perovskite Solar Cells. *ACS Appl. Mater. Interfaces* **2017**, *9*, 11828−11836.

(63) Emara, J.; Schnier, T.; Pourdavoud, N.; Riedl, T.; Meerholz, K.; Olthof, S. Impact of Film Stoichiometry on the Ionization Energy and Electronic Structure of CH3NH3PbI3Perovskites. *Adv. Mater.* **2016**, *28*, 553−559.

(64) Kim, T. G.; Seo, S. W.; Kwon, H.; Hahn, J.; Kim, J. W. Influence of Halide Precursor Type and Its Composition on the Electronic Properties of Vacuum Deposited Perovskite Films. *Phys. Chem. Chem. Phys.* **2015**, *17*, 24342−24348.

(65) Xing, G.; Mathews, N.; Sun, S.; Lim, S. S.; Lam, Y. M.; Gratzel, M.; Mhaisalkar, S.; Sum, T. C. Long-Range Balanced Electron- and Hole-Transport Lengths in Organic-Inorganic $CH_3NH_3PbI_3$. *Science* **2013**, *342*, 344−347.

(66) Tress, W.; Marinova, N.; Moehl, T.; Zakeeruddin, S. M.; Nazeeruddin, M. K.; Grätzel, M. Understanding the Rate-dependent J-V Hysteresis, Slow Time Component, and Aging in $CH_3NH_3PbI_3$ Perovskite Solar Cells: the Role of a Compensated Electric Field. *Energy Environ. Sci.* **2015**, *8*, 995−1004.

(67) Unger, E. L.; Hoke, E. T.; Bailie, C. D.; Nguyen, W. H.; Bowring, A. R.; Heumüller, T.; Christoforo, M. G.; McGehee, M. D. Hysteresis and Transient Behavior in Current-voltage Measurements of Hybrid-perovskite Absorber Solar Cells. *Energy Environ. Sci.* **2014**, *7*, 3690−3698.

(68) Lee, Y. H.; Luo, J.; Son, M.-K.; Gao, P.; Cho, K. T.; Seo, J.; Zakeeruddin, S. M.; Grätzel, M.; Nazeeruddin, M. K. Enhanced Charge Collection with Passivation Layers in Perovskite Solar Cells. *Adv. Mater.* **2016**, *28*, 3966−3972.

(69) Xiong, L.; Qin, M.; Yang, G.; Guo, Y.; Lei, H.; Liu, Q.; Ke, W.; Tao, H.; Qin, P.; Li, S.; Yu, H.; Fang, G. Performance Enhancement of High Temperature SnO_2-based Planar Perovskite Solar Cells: Electrical Characterization and Understanding of the Mechanism. *J. Mater. Chem. A* **2016**, *4*, 8374−8383.

(70) Pérez-del-Rey, D.; Boix, P. P.; Sessolo, M.; Hadipour, A.; Bolink, H. J. Interfacial Modification for High-Efficiency Vapor-Phase-Deposited Perovskite Solar Cells Based on a Metal Oxide Buffer Layer. *J. Phys. Chem. Lett.* **2018**, *9*, 1041−1046.